Geochimica et Cosmochimica Acta 340 (2023) 108–119

Contents lists available at ScienceDirect

Geochimica et Cosmochimica Acta

journal homepage: www.elsevier.com/locate/gca

Genetics, age, and crystallization history of group IC iron meteorites

Hope A. Tornabene [a,b,*], Richard D. Ash [b], Richard J. Walker [b], Katherine R. Bermingham [a]

[a] Department of Earth and Planetary Sciences, Rutgers University, Piscataway, NJ 08854, USA
[b] Department of Geology, University of Maryland, College Park, MD 20742, USA

ARTICLE INFO

Article history:
Received 7 May 2022
Accepted 15 November 2022
Available online 17 November 2022
Associate editor: Frederic Moynier

Keywords:
IC meteorites
Highly siderophile elements
Re-Os isotopes
Fractional crystallization
Hf-W chonometry
Genetics
Nucleosynthesis

ABSTRACT

The IC iron meteorite group is characterized utilizing nucleosynthetic mass-independent isotopic compositions and ^{182}W age constraints, coupled with siderophile element concentration measurements and modeling of crystal-liquid fractionation processes. The six IC irons analyzed, Arispe, Bendego, Chihuahua City, Nocoleche, NWA 2743, and Winburg have indistinguishable Mo and W genetic isotopic compositions and are consistent with derivation from the same parent body, which formed in the non-carbonaceous (NC) nebular reservoir. A pre-exposure μ^{182}W value (parts-per-million deviations in isotopic ratios from terrestrial standards) for the six IC irons of −337 ± 5 corresponds to a metal-silicate segregation age of 1.0 ± 0.4 Myr after calcium-aluminum-rich inclusion (CAI) formation. This age is similar to those determined for other NC iron groups. Siderophile element abundances of the IC irons are generally similar and characterized by minor depletions in the more volatile siderophile elements. Highly siderophile element (HSE) distributions among the IC group suggest that the initial parent body core was S-rich, with preferred model results indicating an initial melt composition with ~ 18 wt% S, 2 wt% P and 0.03 wt % C. Processes in addition to fractional crystallization, such as late-stage parent body modification, possibly as a result of impacts, and subsequent metal-melt mixing, are required within the first 100 Myr of Solar System history to explain the range of HSE abundances.

1. Introduction

Most iron meteorites are believed to be derived from the cores of early-formed planetesimals. Members of an iron meteorite group are presumed to be from a common parent body that underwent melting, differentiation, including core formation, and subsequent crystallization. It is now recognized that asteroidal core formation occurred within the first several Myr of Solar System history, with parent body accretion starting within 1 Myr of formation (e.g., Kruijer et al., 2017). As such, iron meteorites sample some of the earliest-formed bodies in the Solar System and provide valuable insights into the chemical composition and isotopic characteristics of the Solar nebula.

The IC iron meteorite group currently consists of 13 members that were classified based on similar Ni, Ga and Ge concentrations (Scott, 1977). Overall, the group is characterized by minor depletions in the more volatile siderophile elements (e.g., Ga, Ge). Unlike other iron meteorite groups, the IC irons are also characterized by diverse mineral textures, as well as a large range of estimated cooling rates that vary by more than four orders of magnitude (~1 to 10^4 K Myr^{-1}; Scott, 1977). Textures range from coarse octahedrites to recrystallized mineralogies (Buchwald, 1975). Two group IC irons, Nocoleche and Winburg, are classified as mineralogically anomalous, because of their distinctive textures (i.e., irregular patches of Widmanstätten structure; Buchwald, 1975). The IC group is classified as a "magmatic" group, suggesting the members within the group can be related to one another by crystal-liquid fractionation of a common metallic melt (Scott, 1977). Such mineralogical diversity and variable cooling rates are not common in other magmatic iron meteorite groups. This raises the question of whether all of the meteorites grouped as IC formed on the same parent body as part of the same crystallization sequence.

Meteorites that have crystallized from the same parental melt should be characterized by identical nucleosynthetic, or "genetic" isotope compositions, which are inherited from precursor materials from which the parent body formed. These mass-independent isotope heterogeneities have been observed for isotopically diverse siderophile elements such as Mo, Ru and W among iron meteorite groups (e.g., Dauphas et al., 2004; Fischer-Godde et al., 2015; Kruijer et al., 2017; Bermingham et al., 2018). The anomalies likely developed due to incorporation of isotopically diverse presolar materials to the parent bodies, perhaps from distinct nebular reservoirs.

* Corresponding author.
E-mail address: hope.tornabene@rutgers.edu (H.A. Tornabene).

https://doi.org/10.1016/j.gca.2022.11.016
0016-7037/

Previous studies have used the variations in genetic isotope characteristics to identify a dichotomy of meteorites distinguishing between non-carbonaceous (NC) and carbonaceous chondrite (CC) types (e.g., Trinquier et al., 2007; Warren, 2011). Several scenarios have been proposed to explain how the NC-CC dichotomy was established. One possibility is that the NC and CC type meteorites sample distinct nebular reservoirs that were segregated and initially remained isolated by an accreting proto-Jupiter (Warren, 2011; Kruijer et al., 2017). Dynamical modeling by Brasser and Mojzsis, (2020), however, led to the conclusion that Jupiter could not have been responsible for causing the separation of the NC and CC reservoirs. This study proposed that a long-lived pressure maximum created a ringed structure in the early disk which led to the NC-CC dichotomy. Alternatively, Lichtenberg et al. (2021) concluded that the inward and outward movement of the water snow line led to two distinct periods of planetesimals formation, which in turn caused the isotopic and chemical differences between CC and NC materials. Regardless of the true cause of the dichotomy, the Mo, Ru and W genetic isotope characteristics of IC iron meteorites indicate they are of the NC genetic type (Kruijer et al., 2017; Poole et al., 2017; Bermingham et al., 2018; Worsham et al., 2019).

The short lived ^{182}Hf-^{182}W isotope system ($t_{½}$ = 8.9 Myr; Vockenhuber et al., 2004) has proven to be useful in constraining the time scale of iron meteorite parent body accretion and core segregation (e.g., Kruijer et al., 2014a; Kruijer et al., 2017). Among iron groups, the IC irons are of particular interest because Kruijer et al. (2017) reported that the projected pre-cosmic ray exposure ^{182}W/^{184}W ratio for the group overlaps within uncertainties of the initial ratio determined for calcium aluminum-rich inclusions (CAI), which were the first condensates to form in the Solar System (Kruijer et al., 2014b). If correct, this result suggests the IC parent body accreted and differentiated soon after initial formation of solids in the protosolar nebula, well within 1 Ma of CAI formation. The IC group may, therefore, represent the earliest formed planetesimal for which we have samples. If so, chemical and isotopic analysis of the IC group can potentially provide important insights to the earliest stages of the chemical structure and evolution of the Solar System.

This study further examines IC parent body metal-silicate segregation and accretion ages by analyzing multiple meteorites from the IC group using the ^{182}Hf-^{182}W system. Also reported are new chemical and ^{187}Re-^{187}Os isotopic data for IC meteorites. Fractional crystallization modeling the siderophile element compositions of these meteorites is used to generate new constraints on the crystallization history of the IC parent body. It is investigated whether some or all IC irons are related by fractional crystallization, and if the projected parent body composition was chemically distinct relative to later formed parent bodies. Furthermore, newly acquired mass-independent Mo and ^{183}W isotopic compositions are used to assess if meteorites classified as IC were derived from the same genetic reservoir. Particular emphasis is on determining whether the texturally anomalous members of the group were formed from the same mixture of genetic precursors, thereby permitting an origin from the same parent body as other IC irons.

2. Samples

Eleven of the thirteen meteorites currently classified as IC irons were obtained for this study. Eight of the meteorite samples were obtained from the Smithsonian Institution, National Museum of Natural History, USA: Arispe (USNM 2638), Chihuahua City (USNM 853), Mount Dooling (USNM 5713), Nocoleche (USNM 2967), St. Francois County (USNM 130), Santa Rosa (USNM 3046), Union County (USNM 1170), and Winburg (USNM 6390). An additional piece of Nocoleche (ME 1039) was obtained from the Field Museum (Chicago). NWA 2743 was obtained from Arizona Skies Meteorites, Flagstaff, Arizona, USA. Bendego was obtained from the Museu Nacional/UFRJ, Brazil, and Etosha was obtained from the UCLA Meteorite Collection.

3. Analytical Methods

3.1. Laser Ablation ICP-MS

All sample preparation and chemical analyses were carried out at the University of Maryland, USA. The meteorite samples were cut into approximately 100 mg pieces using a water-cooled diamond blade saw. Each piece was polished with carborundum paper and sonicated in ethanol to remove saw blade contamination. Siderophile element concentrations were obtained for 3 to 6 tracks along the polished surfaces by laser ablation analysis using a *New Wave* UP213 ultraviolet laser coupled to a *Thermo-Finnigan Element 2* inductively coupled plasma mass spectrometer (ICP-MS), with a repetition rate of 7 Hz and laser output that was varied to maintain an energy flux of $\sim$ 2–4 Jcm^{-2} (Tornabene et al., 2020). To acquire a representative "bulk" trace element composition, no specific phases were avoided. All data were processed using *LAMTRACE* (Rusk, 2009), applying previously measured concentrations of iron meteorites Hoba, North Chile (Filomena piece) and Coahuila for calibration. Initially, Fe was used as an internal standard for the IC group using accepted values in the literature. Following this, all concentrations were recalculated such that Fe, Ni, and Co concentrations summed to 100 %. This calculation usually corrects for approximately 3 % of the total concentration.

3.2. ^{187}Re-^{187}Os and siderophile element isotopic analysis

The chemical-separation techniques used in this study have been previously published (e.g., McCoy et al., 2011). In brief, bulk sample isotope dilution measurements of the highly siderophile elements (HSE) Re, Os, Ir, Ru, Pt and Pd were performed on 0.02–0.28 g polished pieces using combined ICP-MS and negative thermal ionization mass spectrometry (*N*-TIMS). Each sample was spiked with appropriate amounts of separate ^{185}Re-^{190}Os and ^{191}Ir-^{99}Ru-^{194}Pt-^{105}Pd mixed spikes for isotope dilution. Sample and spike mixtures were sealed and digested in *Pyrex*™ Carius tubes at 230℃ for $\sim$ 24 h, along with 5 mL of high purity concentrated HNO_3 and 2.5 mL of high purity concentrated HCl. After opening the tubes, Os was immediately extracted using a carbon tetrachloride solvent extraction method (Cohen and Waters, 1996), and further purified by microdistillation (Birck et al., 1997). Approximately 100–200 ng of purified Os was loaded onto an outgassed Pt filament with a $Ba(OH)_2$ activator and analyzed as OsO_3^- by *N*-TIMS using standard techniques (Cook et al., 2004). Osmium isotope dilution data were corrected for natural and instrumental mass fractionation by normalizing ^{190}Os/^{188}Os to 3.08271 (Allègre and Luck, 1980).

From the remaining aqueous phase following Os extraction, Re, Ir, Ru, Pt and Pd were separated and purified using anion exchange columns (Rehkämper and Halliday, 1997). Each sample was loaded into a column ($\sim$2 mL of AG 1x8 100–200 mesh resin) in 0.8 M HNO_3, then eluted with 12 mL 6 M HNO_3 for Re and Ru, 12 mL concentrated HNO_3 for Ir and Pt, and 15 mL concentrated HCl for Pd collection. Rhenium and Ru aliquots were further purified using a scaled-down version of the primary anion column. The HSE cuts were dried, taken up in 0.8 M HNO_3, and were analyzed using a *Thermo Neptune Plus* multi-collector ICP-MS using Faraday cup detectors coupled to 10^{11} or $10^{13}\Omega$ resistors. The uncertainties

for Re and Os concentrations are ± 0.1 % (2SD) and the uncertainties for Ir, Ru, Pt and Pd concentrations are < 2 % (2SD).

For high precision mass-independent (unspiked) measurements of Mo, W, Pt and Os, pieces of six IC irons, ranging in mass from 1 to 7 g, were dissolved in 50–100 mL 8 M HCl at 140 ℃ for 48 h in Teflon® beakers. The chemical separation and purification procedures used are published (Walker, 2012; Nagai and Yokoyama, 2014; Worsham et al., 2016; Hunt et al., 2017).

Briefly, one aliquot of the digested sample solution was used for W, Mo, and Pt analysis. This aliquot was dried down and dissolved in 0.4 M HCl – 0.5 M HF and loaded onto a primary anion column with 2 mL AG 1x8 200–400 mesh resin. Tungsten was eluted with 9 M HCl – 1 M HF, Mo was eluted with 6 M HNO_3 – 3 M HF, and Pt was eluted with concentrated HNO_3.

The W aliquot was dried, re-dissolved in 0.4 M HCl – 0.5 M HF and loaded onto a scaled-down version of the primary anion column for further purification. Tungsten was eluted with 9 M HCl – 3 M HF, dried, and dissolved in 1 M HCl – 0.01 M HF. Approximately 1000 ng W was loaded onto an outgassed single Re filament with 1 μL of 5 μg/μL La – 5 μg/μL Gd activator solution. Tungsten was analyzed as WO_3^- by *N*-TIMS using techniques described by Touboul and Walker (2012) and Archer et al. (2017). Mass interferences from ReO_3^- were monitored and corrected. Tungsten isotopic data were corrected for natural and instrumental mass fractionation by normalizing $^{186}W/^{184}W$ to 0.92767 (Völkening et al., 1991). Results of isotopic composition measurements in this study are reported using the μ notation (e.g., W):

$$\mu^{182}W = \left(\frac{\frac{^{182}}{^{184}}W_{sample}}{\frac{^{182}}{^{184}}W_{standard}} - 1\right) * 10^6 \quad (1)$$

The external (2 σ) reproducibility of repeated analyses of the *Alfa Aesar* terrestrial laboratory standard were ± 5 ppm or better for $\mu^{182}W$ and $\mu^{183}W$. Duplicate analyses of Chihuahua City and Winburg are in good agreement at < 5 ppm level.

From the primary column, Mo was dried, re-dissolved in 6 M HCl, loaded onto a scaled-down anion column with ~ 0.3 mL AG 1x8 200–400 mesh resin and eluted with 1 M HCl. This scaled-down anion column elution was repeated twice. Aliquots were dried and re-dissolved in 6 M HCl. A double filament assembly was used for *N*-TIMS analysis. Approximately 1000 ng Mo was loaded onto an outgassed Re filament along with ~ 2 μL of 5 μg/μL $La(NO_3)_3$ activator solution. The same amount of $La(NO_3)_3$ activator was loaded onto the second filament. Molybdenum was analyzed as MoO_3^- by *N*-TIMS (following Worsham et al., 2016). To correct for O interferences, the $^{100}Mo^{18}O^{16}O_2^-$ species was measured using a 10^{13} Ω resistor amplifier. Molybdenum isotopic data were corrected for natural and instrumental mass fractionation by normalizing $^{98}Mo/^{96}Mo$ to 1.453171 (Lu and Masuda, 1994). The maximum external (2 σ) uncertainty of repeated analyses of the *Alfa Aesar* terrestrial laboratory standard analyzed were ± 45 ppm, ± 17 ppm, ± 10 ppm, ± 7 ppm and ± 20 ppm for $\mu^{92}Mo$, $\mu^{94}Mo$, $\mu^{95}Mo$, $\mu^{97}Mo$ and $\mu^{100}Mo$ respectively.

Platinum-196 was used in this study to monitor cosmic ray exposure (CRE) effects on the isotopic compositions of Mo and W. Exposure to cosmic rays in space can lead to the modification of the isotopic compositions of certain elements in a cosmochemical sample. The magnitude of isotopic shift for a given meteorite sample and element depends on the total fluence of cosmogenic effect particles within the sampled domain and the neutron capture cross section of the isotope. Thus, the CRE effect can, in part, reflect the sampling depth from the surface, and the effect can vary between pieces from the same meteorite sample, hence Pt isotopes were measured from the same aliquot as the other isotope systems to ensure accurate CRE corrections. Platinum was eluted from the primary column using concentrated HNO_3 following Mo elution. Subsequent purification follows the procedure described by Hunt et al. (2017) and Hilton et al. (2019). In brief, Pt aliquots from the primary column were dissolved in 2.5 mL 1 M HCl and refluxed over night at 100C. Next, 0.2 M ascorbic acid was added to the solution, and it was loaded onto an anion exchange column with ~ 0.3 mL AG 1x8 200–400 mesh resin and eluted with concentrated HNO_3. This column was repeated once to reduce the Pt/Ir ratio of the samples. Samples were treated with concentrated *aqua regia* and concentrated $HClO_4$ to remove organics and Os. The aliquots were then dissolved in 0.5 M HNO_3 for analysis using a *Thermo Neptune Plus* multi-collector ICP-MS using Faraday cup detectors. Platinum isotopic data were corrected for natural and instrumental mass fractionation by normalizing $^{198}Pt/^{195}Pt$ to 0.2145 (Kruijer et al., 2013). Osmium-189, ^{191}Ir, ^{193}Ir, and ^{200}Hg were used to monitor interferences. For all IC samples, the intensities of ^{191}Ir and ^{200}Hg were below detection limits. The Pt isotope analyses of samples were bracketed by, and normalized to, measurements of an *Alfa Aesar* Pt concentration standard. The average external (2 σ) uncertainty of repeated analyses of the terrestrial laboratory standard analyzed was ± 7 ppm for $\mu^{196}Pt$. High precision Os isotope composition measurements were made for one sample as an additional CRE dosimeter. The Os isolation, purification, and measurement methodologies used were the same as described above, except that the sample was not spiked prior to digestion. The average external (2 σ) uncertainty of repeated analyses of the *Johnson Matthey* terrestrial laboratory standard analyzed were ± 6 ppm for $\mu^{189}Os$.

4. Results

4.1. Composition and textural analysis by laser ablation ICP-MS

The IC irons are characterized by a large range of diverse metallographic structures. For example, some IC irons (e.g., Arispe, Bendego, Santa Rosa) exhibit clustered cohenite [$(Fe, Ni, Co_3)C$] crystals which are not observed in other IC meteorites (Buchwald, 1975). Other IC meteorites (e.g., Chihuahua City, Mount Dooling, and Nocoleche) are characterized by shock melted structures that are distinct from all other IC irons, and most analyzed iron meteorites (Buchwald, 1975). Average elemental concentrations and 2 σ variations for multiple lines of analysis obtained by LA-ICP-MS are presented in Table 1. The heterogeneity observed for some elements (e.g., Cr) can largely be ascribed to heterogeneous distribution of non-metal phases (sulfides, phosphides, chromites and cohenites) that the laser beam encountered. Siderophile elements are typically lower in abundance in these phases compared to the average metal composition. The siderophile element concentrations averaged along an ablation track that intersected one of these non-metal phases, therefore, tended to be lower than the tracks which did not intersect these minerals.

Chondrite normalized bulk element composition data are characterized by broadly similar patterns for most IC irons, and consistent with published data (Fig. 1**; Table SM1**). Our analyses, as with prior analyses, indicate a minor depletion in volatile siderophile elements, such as Ga and Ge, relative to the more refractory siderophile elements. The refractory elements in most of the IC irons are in chondritic relative proportions, although the concentrations of Re, Os and Ir in some of the meteorites are fractionated and their concentration vary over two orders of magnitude. The IC iron meteorites exhibit significant depletions in the multivalent elements V, Cr, P and Zn relative to elements of similar volatility.

4.2. ^{187}Re-^{187}Os and highly siderophile element concentrations

Rhenium-Os isotopic, and bulk HSE concentration data for the IC iron meteorites are reported in Table 2. The HSE concentrations

Table 1
Average elemental concentrations obtained by LA-ICP-MS. Group IC irons are listed from left to right in order of decreasing Re concentration.

	Arispe	Nocoleche (USNM2976)	Nocoleche (ME1039)	Union County	Mount Dooling	Winburg
Re	0.8 ± 0.2	0.8 ± 0.1	0.7 ± 0.2	0.2 ± 0.1	0.1 ± 0.2	0.1 ± 0.1
Os	6.9 ± 0.9	7.8 ± 0.5	7.7 ± 1.7	1.3 ± 0.5	0.4 ± 0.6	0.4 ± 0.1
W	2.0 ± 0.3	1.8 ± 0.5	1.7 ± 0.4	2.2 ± 0.8	2.1 ± 1.4	1.1 ± 0.2
Ir	10.0 ± 1.4	8.3 ± 0.8	7.3 ± 0.1	2.8 ± 0.9	1.1 ± 0.2	1.1 ± 0.1
Mo	7.4 ± 3.1	6.0 ± 1.3	7.0 ± 1.6	7.7 ± 1.8	11.3 ± 1.5	7.3 ± 2.5
Ru	14.0 ± 2.2	10.9 ± 0.8	10.5 ± 0.9	14.8 ± 2.1	12.5 ± 1.5	7.4 ± 1.9
V	3.8 ± 1.0	b.d.	b.d.	3.4 ± 9.2	b.d.	b.d.
Pt	19.3 ± 1.6	16.9 ± 1.8	15.2 ± 0.8	21.3 ± 6.7	16.6 ± 0.5	9.1 ± 1.0
Rh	1.9 ± 0.2	1.6 ± 0.2	1.6 ± 0.1	2.1 ± 0.5	1.9 ± 0.2	1.8 ± 0.3
Ni	6.2 ± 0.7	5.8 ± 0.1	6.6 ± 0.5	5.7 ± 0.7	5.7 ± 1.2	7.6 ± 2.7
Co	0.47 ± 0.02	0.46 ± 0.02	0.46 ± 0.01	0.48 ± 0.05	0.46 ± 0.04	0.46 ± 0.07
Fe[a]	93.0	93.1	96.0	93.4	93.0	92.6
Pd	2.6 ± 0.5	1.8 ± 0.4	1.7 ± 0.1	1.8 ± 0.3	1.9 ± 0.1	3.2 ± 0.5
Cr	84 ± 121	109 ± 211	–	52.0 ± 4.2	61 ± 20	51 ± 37
P	0.2 ± 0.2	0.3 ± 0.2	0.7 ± 0.4	0.3 ± 0.2	0.5 ± 0.7	0.3 ± 0.4
As	5.6 ± 2.2	4.0 ± 1.3	3.9 ± 0.6	4.3 ± 0.8	3.8 ± 0.2	8.8 ± 3.0
Au	0.6 ± 0.1	0.4 ± 0.1	0.6 ± 0.1	0.5 ± 0.2	0.3 ± 0.1	0.8 ± 0.1
Ga	51 ± 4	47 ± 1	50 ± 3	56 ± 7	54 ± 4	51 ± 4
Ge	235 ± 15	137 ± 5.0	148 ± 13	262 ± 69	230 ± 14	217 ± 41
Zn	1.3 ± 0.6	2.0 ± 0.6	–	4 ± 13	1.3 ± 1.4	2.7 ± 3.4
n	*4*	*3*	*4*	*6*	*3*	*3*
	Chihuahua City	Santa Rosa	St Francois County	NWA 2743	Bendego	Etosha
Re	0.03 ± 0.04	0.01 ± 0.02	0.01 ± 0.02	0.01 ± 0.02	0.01 ± 0.01	0.01 ± 0.01
Os	0.1 ± 0.1	0.02 ± 0.03	0.03 ± 0.07	0.05 ± 0.03	0.06 ± 0.06	0.13 ± 0.04
W	0.6 ± 0.4	0.9 ± 0.1	1.2 ± 0.1	0.9 ± 0.1	1.5 ± 0.4	0.6 ± 0.2
Ir	0.1 ± 0.1	0.06 ± 0.03	0.14 ± 0.07	0.15 ± 0.07	0.20 ± 0.03	0.108 ± 0.004
Mo	8.7 ± 2.1	7.9 ± 5.7	6.3 ± 2.9	9.0 ± 3.0	6.3 ± 2.5	7.1 ± 1.5
Ru	4.1 ± 0.2	3.7 ± 1.8	6.5 ± 2.2	4.6 ± 0.8	7.7 ± 1.1	3.6 ± 0.7
V	0.7 ± 1.0	b.d.	b.d.	b.d.	1.8 ± 1.0	b.d.
Pt	4.7 ± 0.9	5.0 ± 2.3	10.1 ± 2.4	6.0 ± 0.6	12.0 ± 0.7	4.2 ± 1.0
Rh	1.6 ± 0.2	1.4 ± 0.4	1.5 ± 0.2	1.6 ± 0.2	2.0 ± 0.3	1.4 ± 0.3
Ni	6.6 ± 0.4	6.3 ± 1.6	4.8 ± 1.6	6.1 ± 1.0	5.6 ± 0.7	6.3 ± 0.5
Co	0.49 ± 0.02	0.49 ± 0.01	0.53 ± 0.04	0.50 ± 0.05	0.48 ± 0.02	0.46 ± 0.03
Fe[a]	92.9	92.9	92.8	92.8	93.1	87.3
Pd	2.1 ± 0.7	2.4 ± 1.3	1.9 ± 1.5	2.4 ± 0.5	2.6 ± 0.3	2.4 ± 0.9
Cr	86 ± 39	115 ± 59	36 ± 29	50 ± 51	44 ± 80	b.d.
P	0.9 ± 0.3	1.0 ± 2.2	0.5 ± 0.6	0.3 ± 0.3	0.13 ± 0.02	2.3 ± 2.0
As	10.8 ± 3.9	9.0 ± 4.8	6.6 ± 0.7	6.4 ± 1.3	9.0 ± 2.4	b.d.
Au	0.6 ± 0.1	0.4 ± 0.1	0.68 ± 0.04	0.7 ± 0.1	0.4 ± 0.1	0.9 ± 0.4
Ga	51 ± 3	49 ± 4	46 ± 3	48 ± 4	54 ± 3	50 ± 8
Ge	208 ± 3	194 ± 56	221 ± 11	202 ± 14	231 ± 8	229 ± 53
Zn	1.2 ± 0.3	1.36 ± 0.02	1.0 ± 0.9	1.7 ± 1.4	1.3 ± 0.8	b.d.
n	*3*	*3*	*3*	*5*	*3*	*4*

Nickel, Co, Fe and P concentrations reported in wt%, all others reported in ppm.
The 2σ values reported were determined from the reproducibility of the number of lines measured (*n*) for each sample.
b.d. Concentrations below detection limits.
[a] Fe data were used as an internal standard.

of the IC group obtained by isotope dilution are on average within 0.2–10 % of values obtained by LA-ICP-MS, however, deviations for some HSE (Re, Os and Ir) range up to 40 %. The isotope dilution measurements access much greater volumes of meteorite and are likely more representative of the bulk composition than the laser ablation analyses. Meteorite NWA 2743 was processed twice for bulk analysis to assess sample heterogeneity and reproducibility. Duplicate concentration determinations of HSE in bulk chunks of NWA 2743 yield percentage differences of ∼ 5 % for Re, Os, Ru and Pt, and ∼ 25 % for Ir and Pd. Duplicate $^{187}Re/^{188}Os$ and $^{187}Os/^{188}Os$ of this meteorite differ from each other outside analytical uncertainties, and have a reproducibility of 4 % and 0.4 %, respectively. These differences are likely due to sample heterogeneity (i.e., non-equivalent distribution of taenite and kamacite).

The fractionation of Re from Os during crystallization of the IC group resulted in a moderate range in $^{187}Re/^{188}Os$ from 0.3852 (Etosha) to 0.9418 (Mount Dooling), and a corresponding range in $^{187}Os/^{188}Os$ from 0.12671 to 0.17170. Two samples, Mount Dooling and Chihuahua City, do not plot within uncertainties of the IC isochron, indicative of minor post-crystallization Re gain or Os loss (Fig. 2). A regression of $^{187}Re/^{188}Os$ *vs* $^{187}Os/^{188}Os$ data for the IC irons (including duplicates but excluding Mount Dooling and Chihuahua City), assuming 0.01 % and 0.15 % uncertainties for $^{187}Re/^{188}Os$ and $^{187}Os/^{188}Os$, respectively, gives an initial $^{187}Os/^{188}Os$ = 0.0962 ± 0.0054 and an imprecise age of 4490 ± 450 Myr, calculated using *ISOPLOT* (Ludwig, 2003). This is broadly consistent with other iron meteorite groups (Walker et al., 2008 [IVB]; McCoy et al., 2011 [IVA]), and indicates minimal post-crystallization open system behavior of the HSE.

Chondrite normalized HSE patterns of the IC irons are characterized by similar features (Fig. 3). The HSE concentrations of the IC irons, with the exception of Nocoleche, are notably fractionated relative to chondritic abundances. By contrast, Nocoleche is characterized by suprachondritic absolute Re, Os, Ir, Ru and Pt abundances that are minimally fractionated in comparison to bulk chondrites, but has a substantial depletion in Pd. Unlike bulk data for most magmatic iron groups, the HSE patterns for some IC meteorites cross, given the ∼ 1 % analytical uncertainties estimated for the concentrations of the HSE (except for Re and Os which are ∼ 0.1 %). Samples within a meteorite group that formed solely by

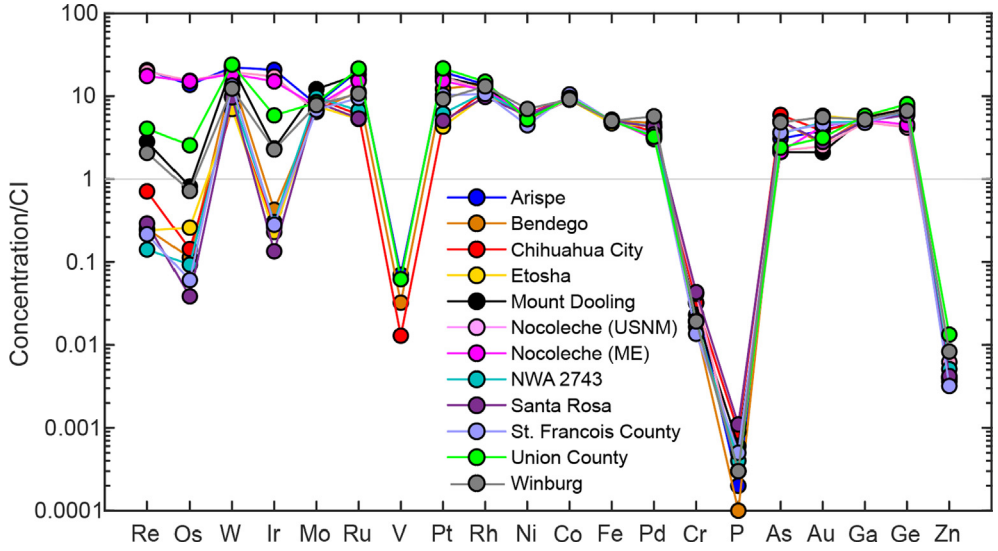

Fig. 1. CI chondrite normalized abundances of siderophile elements for the IC irons. Elements are in order of decreasing 50 % condensation temperatures from left to right.

Table 2
Osmium isotopic and HSE composition data, obtained by isotope dilution, in order of decreasing Re concentration.

Sample	Wt.	Re	Os	Ir	Ru	Pt	Pd	$^{187}Os/^{188}Os$	2σ	$^{187}Re/^{188}Os$	2σ	Δ_{Os}	2 σ
Arispe	0.018	773.8	6737	9566	13,220	18,750	2897	0.13914	0.00010	0.5543	0.0015	−0.6	2.0
Nocoleche (USNM2976)	0.020	657.4	7329	7568	11,220	16,280	2033	0.12942	0.00010	0.4323	0.0015	−0.7	2.0
Union County	0.026	145.6	1022	2270	13,190	18,710	1705	0.15017	0.00010	0.6883	0.0015	−0.2	2.0
Mount Dooling	0.190	71.52	368.0	1198	11,910	17,380	2118	0.17170	0.00010	0.9418	0.0015	2.1	2.0
Winburg	0.020	69.63	375.7	972	6539	8707	2892	0.16490	0.00010	0.8959	0.0015	−1.9	2.0
Bendego	0.056	15.47	139.7	291	10,780	15,340	2269	0.13649	0.00010	0.5343	0.0015	−1.7	2.0
NWA 2743	0.019	10.23	78.72	136	4813	6048	2665	0.14416	0.00010	0.6275	0.0015	−1.4	2.0
NWA 2743 (Replicate)	0.206	9.437	75.63	107	4583	6264	3267	0.14352	0.00010	0.6025	0.0015	0.7	2.0
Etosha	0.066	9.980	124.8	110	3643	4268	2583	0.12671	0.00010	0.3852	0.0015	1.1	2.0
Chihuahua City	0.223	9.774	89.27	125	3773	5174	3185	0.13464	0.00010	0.5280	0.0015	−3.1	2.0
St. Francois County	0.206	5.817	39.64	92	8195	11,320	3140	0.15255	0.00010	0.7095	0.0015	1.3	2.0
Santa Rosa	0.278	4.671	35.68	46	4074	6030	3905	0.14633	0.00010	0.6323	0.0015	0.4	2.0

Unit of weight is in grams (g). Highly siderophile element concentrations are in ppb.
The uncertainties for Re and Os concentrations are ± 0.1 % (2SD) and the uncertainties for Ir, Ru, Pt and Pd concentrations are < 2 % (2SD).

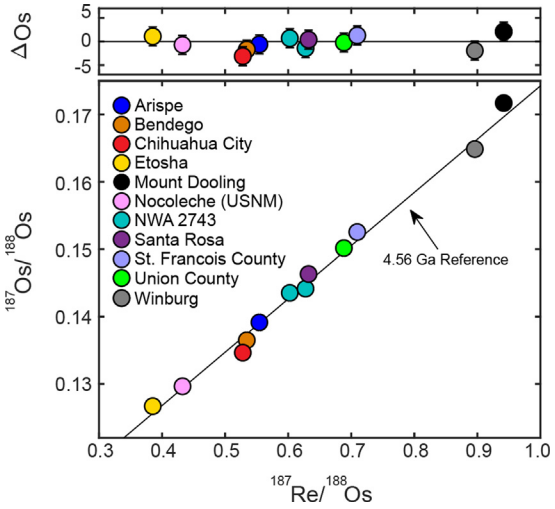

Fig. 2. $^{187}Re/^{188}Os$ *vs*/ $^{187}Os/^{188}Os$ for group IC iron meteorites. Symbols in lower figure are larger than error bars. Upper figure shows $^{187}Re/^{188}Os$ *vs* Δ values (parts per 10,000 deviation from the IC isochron). The error bars represent the combined estimated uncertainties for $^{187}Re/^{188}Os$ and $^{187}Os/^{188}Os$ as discussed in the text.

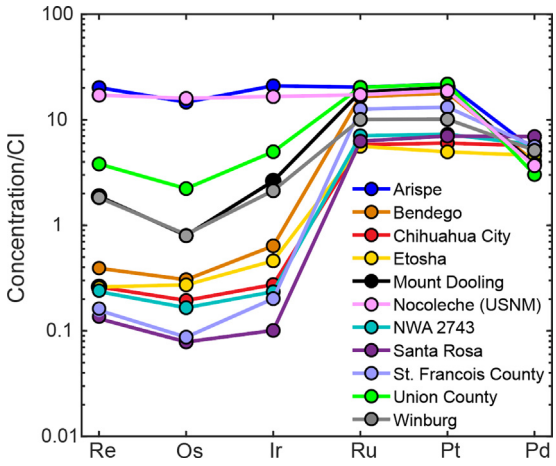

Fig. 3. Bulk CI chondrite normalized abundance plot of HSE obtained by isotope dilution. Orgueil (CI) data from Horan et al. (2003).

simple crystal-liquid fractionation would be expected to have "stacked" HSE patterns with minimal or no crossing of patterns (patterns normally cross between Pt and Pd because of the incom-

patible behavior of Pd, in contrast to the compatible behavior of other HSE). For example, Santa Rosa would be expected to have the lowest concentration of Re, Os, Ir, Ru and Pt, but this is not observed. The crossing of these patterns indicates that simple crystal-liquid fractionation alone cannot relate the IC irons to one another.

4.3. Cosmic ray exposure effects

Exposure to cosmic rays in space can lead to modifications to W, Mo and Ru isotopic compositions resulting from secondary neutron capture (e.g., Wittig et al., 2013). Platinum isotopic compositions, used for monitoring neutron capture effects, are presented in Table 3**.** Chihuahua City has μ^{196}Pt values which are not resolved from the Pt terrestrial standard, therefore, the Mo and W isotopic compositions of this meteorite require no corrections for CRE. Arispe, Bendego, Nocoleche (ME), NWA 2743 and Winburg exhibit μ^{196}Pt values ranging from + 10 ± 3 to + 60 ± 6 (Fig. 4**)**. The μ^{196}Pt values for these meteorites are resolved from the terrestrial standard, reflecting moderate CRE effects. The Os isotopic composition for Arispe was analyzed, with a μ^{189}Os value of −37 ± 6. This μ^{189}Os value is resolved from the Os terrestrial standard, and consistent with the respective, anomalous μ^{196}Pt value.

4.4. Molybdenum and W isotopic compositions

The measured Mo isotopic data for Arispe, Bendego, Chihuahua City, NWA 2743, as well as for the anomalous Winburg and Nocoleche are provided in Table 4. These data are similar to data for IC irons Arispe, Bendego, Mt. Dooling and Chihuahua City reported previously (Burkhardt et al., 2011; Poole et al., 2017; Kruijer et al., 2017; Worsham et al., 2017; 2019; Spitzer et al., 2020; **Table SM2**).

The effects of CRE on Mo isotopic ratios have been discussed by Worsham et al. (2017), Yokoyama et al. (2019), and Spitzer et al. (2020). Corrections to achieve a pre-exposure isotopic composition for an iron meteorite group can be obtained by two methods. One, by regressing the correlations between μ^{i}Mo and μ^{196}Pt (or μ^{189}Os) to obtain the pre-exposure values where the regression lines intersect the μ^{196}Pt (or μ^{189}Os) value of 0. Second, by correcting the measured Mo data for individual meteorites within a group using the measured μ^{196}Pt (or μ^{189}Os) value projected to 0, assuming common μ^{i}Mo *vs* μ^{196}Pt slopes, then averaging the results. The linear regressions of IC μ^{196}Pt *vs* Mo data are shown in **Fig. SM1**. Values obtained by both methods are reported in Table 4 and shown in **Fig. SM2**. The pre-exposure μ values, calculated by the linear regressions, for the IC irons, Arispe, Bendego, Chihuahua City, Nocoleche (ME), NWA 2743, and Winburg obtained here are: +77 ± 18, +85 ± 20, +36 ± 5, +21 ± 4 and + 17 ± 8 for μ^{92}Mo, μ^{94}Mo, μ^{95}Mo, μ^{97}Mo and μ^{100}Mo, respectively. These values are in good agreement with the values reported by Spitzer et al. (2020).

Table 3
Platinum isotopic data obtained by MC-ICP-MS.

Sample	n	μ^{196}Pt	2σ
Arispe	8	+41	7
Bendego	3	+60	6
Chihuahua City	4	−2	6
Chihuahua City (replicate)	2	+3	4
Nocoleche (ME1039)	3	+12	6
NWA 2743	2	+10	3
Winburg	3	+51	2
Winburg (replicate)	4	+50	9

n refers to the number of analyses from the same solution. The reported values are the averages for each sample. Uncertainties reflect the largest 2SD (n < 4) of the standards run during an analytical campaign or 2SE (n ≥ 4) of the sample values.

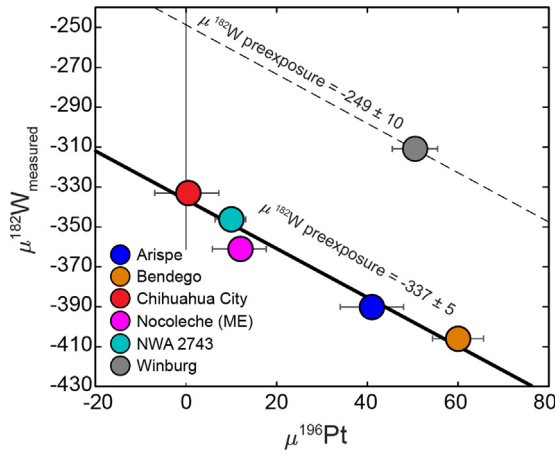

Fig. 4. μ^{196}Pt *vs* μ^{182}W correlation resulting from cosmic ray exposure effects. The solid black line is a linear regression calculated for the IC irons using *ISOPLOT*. The pre-exposure ^{182}W values are defined at μ^{196}Pt = 0. The black dashed line is the calculated regression for Winburg using the same slope of −1.22 ± 0.16 with errors propagated through the calculation.

The measured μ^{182}W and μ^{183}W values for the IC irons are reported in Table 5. Arispe, Bendego, Chihuahua City, Nocoleche (ME), NWA 2743, and Winburg exhibit a narrow range of μ^{183}W values of −3 ± 5 to + 4 ± 5, averaging 1 ± 2 (2SE). The individual measured values for these samples are indistinguishable from the terrestrial standard, therefore, no nucleosynthetic correction to ^{182}W values are required for these meteorites.

The measured μ^{182}W isotopic compositions for Arispe and Bendego are in good agreement with the values reported by Kruijer et al. (2017) (**Table SM4**). The average μ^{182}W value for Chihuahua City of –333 ± 5, measured in this study, however, differs from the measured μ^{182}W value of −352 ± 6 reported by Kruijer et al. (2017). As with Mo isotopes, a pre-exposure μ^{182}W value can be obtained by regression of μ^{196}Pt *vs* μ^{182}W assuming a slope of −1.32 ± 0.06 (Kruijer et al., 2017). The pre-exposure μ^{182}W value calculated for Chihuahua City (this study) is –332 ± 11, which is unresolved from the pre-exposure μ^{182}W value calculated from Kruijer et al. (2017) of −343 ± 11, with analytical uncertainties propagated through the calculations.

A pre-exposure μ^{182}W for the IC irons is obtained by regression of the data with corresponding μ^{196}Pt values (Fig. 4). The μ^{196}Pt *vs* μ^{182}W regression of five IC irons, including duplicates, but excluding the anomalous Winburg, yields a pre-exposure μ^{182}W group value of −336 ± 5. This value overlaps, within uncertainty, to the pre-exposure value calculated by averaging the individually corrected pre-exposure values for the five IC irons (including duplicates) of −337 ± 5. Both pre-exposure μ^{182}W values for these IC irons overlap, within uncertainties, to the −345 ± 4 pre-exposure value reported by Kruijer et al. (2017). The CRE uncorrected μ^{182}W value for Winburg is −311 ± 5 and plots above the Pt-W correlation defined by Arispe, Chihuahua City, Bendego, Nocoleche, and NWA 2743. Applying the same Pt-W correlation slope as for the other IC irons, and propagating errors, projection of Winburg to a μ^{196}Pt value of 0, gives a pre-exposure μ^{182}W value of −249 ± 10 (Fig. 4**;** Table 5**)**.

5. Discussion

5.1. Parent Body Genetics

Before considering physical processes that may relate the IC irons to one another, it is important to first assess whether genetic isotopic compositions indicate if any meteorites from the group

Table 4
Measured Mo isotopic compositions for IC irons.

Sample	n	μ^{92}Mo	2σ	μ^{94}Mo	2σ	μ^{95}Mo	2σ	μ^{97}Mo	2σ	μ^{100}Mo	2σ
Arispe	2	+107	45	+83	17	+28	17	+23	7	+27	20
Bendego	4	+117	45	+89	17	+24	10	+14	10	+45	21
Chihuahua City	6	+71	19	+81	8	+34	5	+21	4	+16	8
Nocoleche (ME1039)	3	+124	45	+116	17	+52	17	+26	16	+29	20
NWA 2743	4	+97	45	+83	17	+33	10	+18	7	+25	20
Winburg	4	+96	45	+87	17	+37	10	+26	7	+19	20
IC Average[a]	6	+77	18	+85	20	+36	5	+21	4	+17	8
IC Average[b]	6	+117	22	+99	12	+46	8	+23	4	+23	7

n refers to the number of analyses (using a new filament assembly for each analysis) of purified Mo from a single digestion. The reported values are the averages of individual analyses for each sample. Uncertainties reflect the 2SD of repeated analyses or the 2SD of the standards, whichever is largest. The uncertainties for Chihuahua City reflect the 2SE of repeated analyses.

[a] Averages calculated from the μ^{i}Mo *vs* μ^{196}Pt regression calculated using *ISOPLOT* using the projected intercept at μ^{196}Pt = 0 (**Fig. SM1**).

[b] Averages calculated from the individually corrected values using the slope of the IIAB iron meteorites reported by Spitzer et al. (2020).

Table 5
Measured W and calculated pre-exposure isotopic compositions and model ages for the IC irons.

Sample	n	$\mu^{182}W_{Measured}$	2σ	$\mu^{183}W_{Measured}$	2σ	$\mu^{182}W_{Corr.}$	2σ	ΔT_{CAI}	2σ
Arispe	1	−390	5	+3	5	−339[b]	12[b]	0.9	1.0
Bendego	1	−406	4	−2	4	−331[b]	12[b]	1.7	1.0
Chihuahua City	2	−333	5	+4	5			1.4	0.2
Nocoleche (ME1039)	1	−361	5	−1	5	−346[b]	10[b]	0.2	0.8
NWA 2743	1	−346	6	−1	5	−334[b]	7[b]	1.4	0.6
Winburg	2	−311	4	0	6	−249[b]	10[b]	12.7	0.9
Group Regression Pre-exposure[a]						**−337**	**5**	**1.0**	**0.4**

For analyses where n = 1, n refers to the number of analyses of purified W from a single digestion. For analyses where n = 2, n refers to the average of two analyses of purified W from two separate digestions of the same meteorite piece.
Uncertainties for the measured values reflect the 2SD of the standards run during an analytical campaign.

[a] The group regression pre-exposure $\mu^{182}W_{Corr.}$ value, and associated uncertainty, was calculated from the μ^{196}Pt *vs* μ^{182}W correlation using *ISOPLOT*.

[b] The $\mu^{182}W_{Corr.}$ values were calculated using the slope and intercept of the μ^{196}Pt *vs* μ^{182}W correlation. The uncertainties associated with the corrections were propagated through into the uncertainties for the model age (ΔT_{CAI}) calculated using Eq. SM1.

formed from a different genetic mixture of presolar components. This would require an origin on a different parent body. Molybdenum and W isotopes were created via the *p*-, *r*-, and *s*-processes. Consequently, their distinctive bulk meteorite nucleosynthetic isotope signatures are useful for assessing genetic relations within and between iron meteorite groups. Our new μ^{i}Mo (CRE corrected) and μ^{183}W data for Arispe, Bendego, Chihuahua City, NWA 2743, as well as the texturally anomalous Winburg and Nocoleche (ME) are uniform, within analytical uncertainties (Fig. 5). These results are consistent with derivation of Arispe, Bendego, Chihuahua City, Nocoleche, NWA 2743, and Winburg from an isotopically uniform nebular reservoir. These data are permissive of the interpretation that the samples were derived from the same parent body.

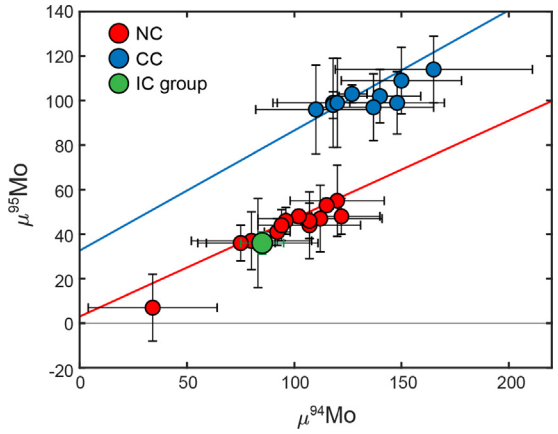

Fig. 5. Plot of μ^{94}Mo *vs* μ^{95}Mo for iron meteorites using data from Table 4 (averages calculated from the individually corrected values using the intercept at μ^{196}Pt = 0 from μ^{i}Mo *vs* μ^{196}Pt) and group averages reported by Bermingham et al. (2018), Worsham et al. (2019), Hilton et al. (2019), Yokoyama et al. (2019) and Spitzer et al. (2020). The NC type meteorites include group averages of IC, IIAB, IIIAB, IIIE and IVA. The CC type meteorites include group averages of IID, IIF, IIIF, IVB and SBT. The blue line is the NC linear regression taken from Budde et al. (2019) and the red line is the linear regression from Spitzer et al. (2020).

The NC-CC type meteorites define what appear to be distinct *s*-process mixing lines on a μ^{94}Mo *vs* μ^{95}Mo plot (Fig. 5; Budde et al., 2016; Poole et al., 2017; Worsham et al., 2017; Bermingham et al., 2018; Budde et al., 2019; Spitzer et al., 2020; Stephan and Davis, 2021). The CC line is offset above the NC line, which may be a result of a minor *r*-process (or *p*-process) enrichment or variations in the isotope makeup of the *s*-process contribution to meteorite samples. The CRE corrected average μ^{92}Mo, μ^{94}Mo, μ^{95}Mo, μ^{97}Mo and μ^{100}Mo values for the IC irons in this study are + 77 ± 18, +85 ± 20, +36 ± 5, +21 ± 4 and + 17 ± 8, respectively, and are consistent with an NC origin, as suggested by prior studies (e.g., Kruijer et al., 2017; Poole et al., 2017). The inferred pre-exposure Mo isotopic compositions of the IC group are also identical, within uncertainties, to the pre-exposure values determined for the NC type IVA iron meteorite group (Worsham et al., 2017).

5.2. Radiogenic W isotope compositions

Previous studies have interpreted the sub-chondritic $^{182}W/^{184}W$ ratios in most iron meteorites to reflect the early timing of metal segregation on their parent bodies. The pre-exposure μ^{182}W value of −337 ± 5 for the IC group determined here corresponds to a ^{182}W model age of 1.0 ± 0.4 Myr after CAI, assuming precursor materials with a carbonaceous chondrite-like Hf/W (see supplementary materials for details). This finding is similar to the

pre-exposure value of −345 ± 4 value reported by Kruijer et al. (2017), which is equivalent to a model age of 0.3 ± 0.5 Myr. The new age overlaps within uncertainty of all other NC type magmatic iron meteorite groups (Kruijer et al., 2017) and is resolved from and younger than the age of CAI.

The anomalous IC iron, Winburg, plots above the calculated μ^{196}Pt-μ^{182}W regression for the other IC irons (Fig. 4). While Winburg, may be genetically linked to the other IC irons, as discussed above, it exhibits a more radiogenic, projected pre-exposure μ^{182}W value, consistent with a metal-silicate closure age of 12.7 ± 0.9 Myr after CAI. This suggests that while it may have formed on the same parent body as the IC irons, it was created either as a result of a later-stage metal segregation process or it was modified by a subsequent impact event on the IC parent body that led to metal-silicate interaction and equilibration. Although there is minimal mineralogical characterization of Winburg, it has been described as a mass of kamacite crystals with veins of hydrated iron, which penetrate into the interior of the meteorite mass (Buchwald, 1975; Rudge, 1914). Winburg may, therefore, provide evidence of at least one, late-stage, impact that resulted in a metal-silicate equilibration process on the IC parent body more than 10 Myr after formation. This is consistent with the observations from Scott et al. (1977), which speculated that an event after crystallization is needed to explain the vastly different mineralogy and cooling history of this meteorite compared to the other IC meteorites.

5.3. Re-Os isotopic system

The IC irons plot on or near a primordial 4.56 Ga reference isochron, indicating that the IC suite, and the two anomalous meteorites, originated from bodies that were generally closed systems and their HSE abundances reflect those at the time of, or within a few tens of Myr of, the crystallization ages. Chihuahua City and Mount Dooling do not plot within uncertainties of the primordial isochron but are only offset by −3.1 and + 2.1 %, respectively. As such, they likely have absolute HSE abundances that reflect only minor loss or gain of Re and Os. These minor offsets would not affect the fractional crystallization modeling discussed below.

5.4. Crystallization models

The uniform Mo and ^{183}W isotopic compositions for the IC irons analyzed in this study are permissive of their formation on the same parent body. The HSE patterns of the IC group are broadly consistent with fractional crystallization because the concentrations of Re, Os, Ir, Ru, and Pt, normally characterized by solid metal-liquid metal D values greater than 1 (where D values are solid/liquid concentration ratios), decrease in metal as crystallization proceeds, while Pd (normally characterized by solid metal-liquid metal D values < 1), increases. Here, appropriate solid metal-liquid metal D values for the HSE are calculated using the parameterization method refined by Chabot et al. (2017) and discussed in detail in Tornabene et al. (2020). The parameterization depends on the mole fractions of S, P and C present throughout the crystallization sequence. The initial abundances of S, P and C are used as the main input variables to calculate D values that can best account for the range of HSE concentrations of the IC group.

The initial P content of the IC parent body is constrained by dividing the average P of the least evolved (highest Re concentration) IC iron (Arispe) by the constant D_o value for P of 0.1 (where D_o is the solid metal-liquid metal D value in the Fe-Ni-S, Fe-Ni-P and Fe-Ni-C systems; Chabot et al., 2017). This method suggests an initial P content of approximately 2 wt%. Hirschmann et al. (2021) estimated an initial C content for the IC group of approximately 0.03 wt%. As has been done for other iron meteorite groups (e.g., Wasson, 1999; Chabot, 2004; Tornabene et al., 2020), an estimation of initial bulk S content from the Ga and Ge *vs* Au trends was attempted (**Fig. SM3**). There is no single set of initial parameters, however, that fits all IC HSE data. The best fits to the data are achieved with relatively high initial S contents between 13 wt% and 23 wt%. Due to the large range in possible initial S contents resulting from this type of model, we explore initial S contents by collectively modeling the HSE for systems with 13, 18 and 23 wt% S.

Chabot and Zhang (2022) proposed a model that incorporates changing solid metal HSE concentrations as a result of the crystallization of troilite from trapped melt. In a crystallizing core, S will become concentrated in the liquid metal phase and any trapped metal melt will eventually solidify into troilite and solid metal. The HSE have a low solubility in troilite and will become enriched in the remaining solid metal that crystallizes from the trapped liquid. This model, coupled with similar modeling approaches (e.g., Walker et al., 2008), was applied to the IC group.

The behavior of Re and Os are considered first as they are measured with higher precision than the other HSE, and the measured concentrations represent conditions of initial formation, as required by the generally well behaved Re-Os isotopic systematics of the IC meteorites. Further and most importantly, it is probable that their initial concentration ratio was within the chondritic range, as both elements are highly refractory. As the IC iron with the highest Re concentration, Arispe is assumed to represent the earliest formed solid to crystallize of the available meteorites from this group. Model solid metal and trapped metal evolution tracks of Re concentration *vs* Re/Os with data for the IC irons are shown in Fig. 6. Here, trapped metal refers to the solid metal that crystallizes from trapped melt containing troilite. Model evolution tracks of equilibrium solids and trapped metal, assuming perfect fractional crystallization and initial S contents of 13, 18 and 23 wt%, are defined as models A, B and C, respectively. For these models, initial P and C contents (2 and 0.03 wt%, respectively) were held constant while S, along with initial concentrations of Re and Os (and all other HSE), were varied in order to model Arispe as the earliest formed solid. The initial melt abundances of Re and Os for each model were adjusted to have Arispe plot on the solid track, and the Re/Os of the initial liquid composition to be within the range of chondrites (0.82 to 0.92; Horan et al., 2003; Fischer-Gödde et al., 2010).

In a crystallizing core, several different mixing processes can occur: (1) mixing of equilibrium solids and liquids (or trapped metallic liquid), (2) disequilibrium mixing of solids and liquids (or trapped metallic liquid) and (3) equilibrium mixing of early formed solids and evolved trapped liquids (or trapped metallic liquid). The IC irons can be loosely categorized into two groups defined by their Re concentrations. Arispe, Union County, Mount Dooling, Nocoleche, and Winburg represent the high Re abundance group, while Bendego, Chihuahua City, Etosha, NWA 2743, Santa Rosa and St. Francois County represent the low Re abundance group. The differences between the high and low Re abundance irons may be understood if the low abundance Re irons were formed as variable mixtures of equilibrium solid and trapped metal. This scenario is best explained by mixing between early formed solids (high Re and Os) and evolved trapped metal (lower Re and Os). In a crystallizing core, an infinite number of different mixing scenarios are possible. For simplicity, in models A, B and C, we model the low abundance group as mixtures of an early formed solid generated following < 1 % fractional crystallization with an evolved trapped metal present following 27, 9 and 2 % fractional crystallization, respectively. Cook et al. (2004) suggested that this type of mixing could have been a result of an injection of liquids into a solid core following an impact disruption of the

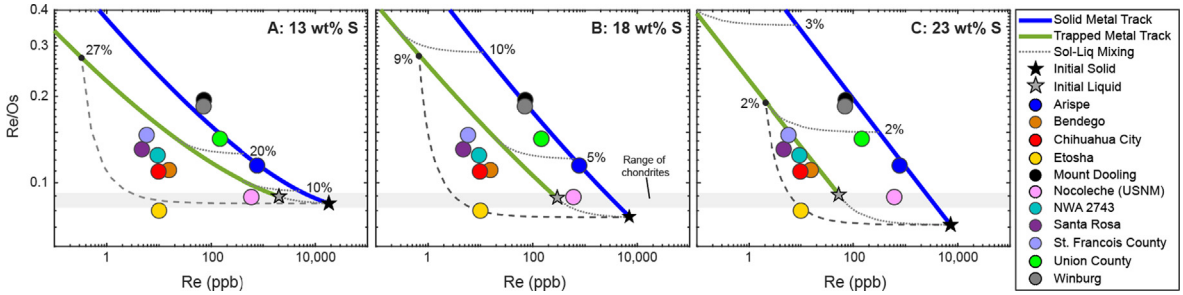

Fig. 6. Re-Os fractional crystallization models A, B and C for parameters discussed in the text. The blue and green lines are calculated solid and trapped metal tracks, respectively. The dotted grey lines are calculated mixing curves connecting the solid and trapped metal tracks. The dashed grey lines are calculated mixing curves between early formed solids and evolved trapped metals. The black and grey stars are the starting solid and liquid composition of the parent body, respectively. The grey area is the range of chondrites.

parent body. This mechanism is consistent with the conclusions of Scott (1977), who suggested a collision soon after IC core crystallization that fragmented and dispersed some IC irons.

Model A (13 wt% S) generates the composition of Arispe as the first solid to crystallize after approximately 17 % fractional crystallization (i.e., 17 % of the core has crystallized). Both Arispe and Union County fall along the solid track and represent equilibrium solids crystallized from the parental melt. Mount Dooling and Winburg fall to the right of the solid track and cannot be accounted for by this model. The low Re abundance group (excluding Etosha) and Nocoleche can be modeled as mixtures of an early formed solid formed following < 1 % fractional crystallization with an evolved trapped metal present following 27 % fractional crystallization. Etosha, however, falls below the early solid/evolved trapped metal mixing line and is not consistent with this crystal-liquid fractionation model.

Model B uses 18 wt% initial S and can successfully account for the high Re abundance group as equilibrium solids. Similar to model A, all of the low Re abundance group falls to the left of the solid track but can represent variable mixtures of early solids/evolved trapped metal. Etosha is modeled as an early formed solid following < 1 % fractional crystallization with an evolved trapped metal present following 9 % fractional crystallization.

Model C utilizes an initial S content of 23 wt% and produces the largest spread in the calculated solid and trapped metal tracks. As such, model C can successfully account for almost all IC irons (excluding Etosha, Santa Rosa and Chihuahua City) as variable mixtures of equilibrium solid and trapped metal mixtures. Similar to model B, Etosha would represent mixtures of an early formed solid formed following < 1 % fractional crystallization with an evolved trapped metal present following 2 % fractional crystallization.

Modeling of early formed solids and evolved trapped metal mixing can explain the Re and Os concentrations of the low abundance group for models B and C only. In model A, Etosha falls below the early solid/evolved trapped metal mixing line and Mount Dooling and Winburg remain to the right of the solid track. Model A cannot account for the HSE concentrations of the IC group and will not be discussed further with respect to modeling the other HSE.

To summarize, model B is successful at accounting for most of the low Re abundance group as some combination of mixed early solids and evolved trapped metal, with Etosha's Re and Os concentrations corresponding to a mixture of a solid formed after < 1 % crystallization and a trapped metal formed after 9 % crystallization. Model C can account for nearly all samples of the high Re abundance group as equilibrium solids and nearly all the low Re abundance group as equilibrium liquids. In model C, Etosha would represent a mixture of a solid formed after < 1 % crystallization and a trapped metal formed after 2 % crystallization.

Next, we consider the behavior of Pt and Os because, if it is assumed that meteorites formed from an initial melt with chondritic Re/Os, then it is likely the initial liquid would also have chondritic Pt/Os. The Pt concentrations of the initial liquid were iterated after Re and Os to attain an initial liquid composition with Pt/Os within the range of chondrites (1.4 to 2.5; Horan et al., 2003). Fig. 7 presents modeled results of Pt-Os systematics for Models B and C using the same parameters discussed above. For both Models B and C, all IC irons plot between the solid and trapped metal tracks, suggestive of simple solid-trapped metal equilibrium mixing. Similarly, modeled results for Re *vs* Ir, Ru and Pd (**Fig. SM4**), indicate that most IC irons can be successfully modeled by simple solid-trapped metal equilibrium mixing. Modeling of Re *vs* Ir, Ru and Pd and Pt *vs* Pt/Os is inconsistent with models of Re *vs* Re/Os because modeling of the latter requires mixing of early formed solids with evolved trapped metal while the former only requires simple solid-trapped metal equilibrium mixing. The discrepancies between the different model results are likely not a result of post-crystallization disturbance of Re, as deviations of some individual meteorites from a primordial isochron indicate loss or gain or only a few percent Re (or Os). More likely, the discrepancies are the result of modest inaccuracies in the D values used in the models.

The relative amounts of fractionation (i.e., 1–10 %) required to account for all IC irons, is consistent throughout all HSE modeling (for both Models B and C). Consequently, the only discernable differences between Models B and C, is the Re-Os systematics, degree of crystal-liquid fractionation, and the composition of the initial liquid from which the IC irons crystallized. In order to choose the best fit model to the meteorite data, we explore the calculated initial liquid compositions generated from Models B and C.

The IC parent body initial melt concentrations of the other HSE, calculated from models A, B and C, are given in Table 6, along with estimated initial HSE and S contents for other magmatic groups for comparison. Results are shown in Fig. 8 along with the patterns representative of average carbonaceous and ordinary chondrites (Horan et al., 2003). The initial melt concentration pattern calculated from Model C falls below the average HSE composition of both ordinary and carbonaceous chondrites. This sub-chondritic parent body composition is a major failing of this model, as it is normally assumed that the parent bodies of iron meteorites are characterized by bulk compositions with HSE abundances roughly equivalent to those measured in bulk samples of ordinary or carbonaceous chondrites. Core formation concentrates HSE, so extraction of a high percentage of all HSE in the body into a segregated mass of the body that is only 5–30 % of that of the entire body will always lead to considerable enrichment in initial core liquids, compared to bulk chondrites.

Model B's calculated initial melt composition of the IC parent body is characterized by broadly chondritic relative abundances

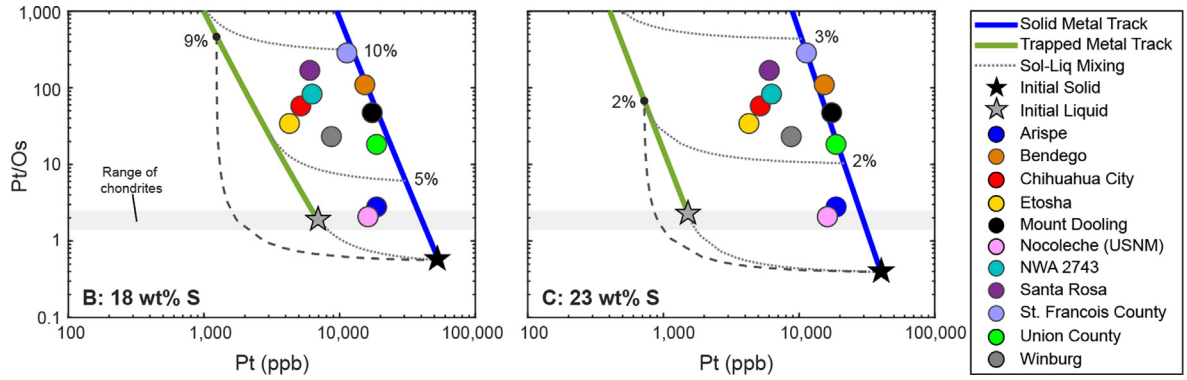

Fig. 7. Pt-Os fractional crystallization models B and C for parameters discussed in the text. The blue and green lines are calculated solid and trapped metal tracks, respectively. The dotted grey lines are calculated mixing curves connecting the solid and trapped metal tracks. The dashed grey lined are calculated mixing curves between early formed solids and evolved trapped metals. The black and grey stats are the starting solid and liquid composition of the parent body, respectively. The grey area is the range of chondrites.

Table 6
Calculated initial concentrations of HSE (in ppb) for the parameters discussed in the text and S and parent body HSE concentrations from the literature.

	S (wt%)	Re	Os	Ir	Ru	Pt	Pd
IC Model A	13	1300	14,500	8000	10,000	14,000	2400
IC Model B	18	150	1700	1700	2400	3200	2100
IC Model C	23	20	220	200	500	600	2100
Non-carbonaceous							
IIAB [f]	17	260	2900	2900	4800	6500	2100
IIIAB [f]	12	260	2800	2800	4400	5900	3100
IVA[c]	6	295	3250	2700	3900	5900	4500
Carbonaceous							
IIC [a]	8	280	3350	3050	4340	6070	5300
IID [f]	10	370	4400	4100	6300	8000	4300
IIF [f]	13	355	4200	4200	6800	8200	4250
IIIF [f]	5	275	3600	3100	4300	6100	4000
IVB[b]	1	2800	37,000	27,000	27,400	29,500	8600
SBT[d]	7	770	9400	8500	13,000	16,000	8400

[a] Data from Tornabene et al., (2020); [b] Data from Walker et al. (2008); [c] Data from McCoy et al. (2011); [d] Data from Hilton et al. (2019), SBT – South Byron Trio; [e] Data from McCoy et al. (2019); [f] Data from Hilton et al. (2022).

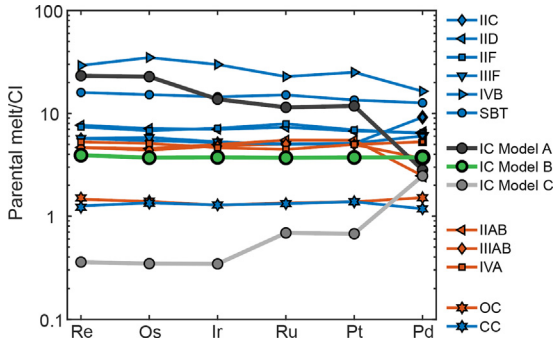

Fig. 8. Calculated HSE concentrations for magmatic iron meteorite groups using the data in Table 6, normalized to CI chondrite Orgueil (Horan et al., 2003). Ordinary (OC) and carbonaceous (CC) chondrite data from Horan et al. (2003). IC Model B (green circles) is the preferred model in this study.

of HSE, and the range of concentrations are similar to estimated parental melt compositions of other magmatic iron meteorite groups (e.g., Hilton et al., 2022). We conclude that model B best represents the evolutional composition of the IC parent body, and it is our preferred model.

Based on the Re-Os concentration data, we conclude that the IC group was likely formed by mixing processes in addition to fractional crystallization. Further, there is evidence (e.g., $\mu^{182}W$ value of Winburg) that the IC core experienced late-stage parent body modification, occurring within the first 100 Myr of Solar System history.

The average HSE composition of ordinary chondrites is assumed to be a proxy for the starting concentration of the IC parent body because ordinary chondrites are of NC type and are commonly characterized by relatively high S abundances (Schrader et al., 2010; Warren, 2011). As such, the concentrations of HSE estimated for the IC group initial core is approximately 4 times higher than the ordinary chondrite average. Assuming ~ 99 % of HSE were extracted into the core, mass balance indicates the IC core would have comprised ~ 25 % of the mass of the body. The estimated initial HSE concentrations of the IC group are comparatively lower than those of the other NC and CC type groups. Assumption of a greater proportion of metallic iron in the IC core would result in lower concentrations of HSE. This is consistent with the IC parent body forming in a relatively more reducing environment than that of the IIAB, IIIAB and IVA (NC type) parent bodies. The NC nebular reservoir is commonly envisioned as having been a more reducing environment compared to the CC reservoir (Hilton et al., 2022).

Of the iron meteorite groups listed in Table 6, the IVA irons are the only other group that shows evidence of complex core crystallization (e.g., collision events). The measured cooling rates for the IVA irons range from ~ 100 to 5,000 K Myr^{-1} (Goldstein et al., 2014; Scott, 2020). Rubin et al. (2022) suggested that the range in cooling rates is a result of crystallization in a metallic core surrounded by a thin silicate mantle. The range of estimated cooling rates for the IC irons are two orders of magnitude greater than

the range of the IVA irons, indicating that either the IC core was surrounded by an even thinner silicate mantle, relative to the IVA mantle, or the size of the IC core was relatively larger than that of the IVA core, so that the IC irons would have been dispersed on a relatively larger scale. Although the IVA and IC irons differ greatly in their chemical compositions, especially given that the IVA group is highly depleted in volatile siderophile elements, it is intriguing that these two groups share certain similar formation process, as well as identical Mo and W isotopic compositions.

6. Conclusions

Despite their textual diversity, Arispe, Bendego, Chihuahua City, Nocoleche, NWA 2743 and Winburg have identical Mo and W genetic isotopic compositions, as well as similar chemical compositions, indicating formation from the same parent body from an NC type nebular reservoir similar to other NC parent bodies. The radiogenic W isotopic composition of the anomalous IC iron, Winburg, suggests formation on the same parent body but in a separate metal segregation event.

The pre-exposure μ^{182}W value of five IC irons (Arispe, Bendego, Chihuahua City, Nocoleche, and NWA 2743) of −337 ± 4 yields a ^{182}W model age of 1.0 ± 0.3 Myr after CAI formation. The siderophile element abundance patterns of IC iron meteorites are broadly similar. To account for HSE abundance variations, a preferred initial parental melt composition is estimated to contain ∼ 18 wt% S, 2 wt% P and 0.03 wt% C. Despite the similarities in HSE patterns, the abundances of these elements in the IC group cannot be accounted for solely by simple fractional crystallization and require solid–liquid mixing processes to account for the variations. Some of the mixing processes were likely initiated by post-crystallization impacts, which also affected textures and cooling rates.

Data availability

Data will be made available on request.

Declaration of Competing Interest

The authors declare that they have no known competing financial interests or personal relationships that could have appeared to influence the work reported in this paper.

Acknowledgments

Funding for this work was provided by NASA Emerging Worlds grant 80NSSC20K0335 (to RJW) and is gratefully acknowledged. The authors thank the Smithsonian Institution National Museum of Natural History, the Museu Nacional/UFRJ, Brazil, and the late John Wasson and the UCLA Meteorite Collection for providing us with meteorite samples. The authors also thank Nao Nakanishi and Jan Hellmann for their help with collecting ICP-MS measurements.

Appendix A. Supplementary material

Supplementary material to this article can be found online at https://doi.org/10.1016/j.gca.2022.11.016.

References

Allègre, C.J., Luck, J.M., 1980. Osmium isotopes as petrogenetic and geological tracers. Earth Planet. Sci. Lett. 48 (1), 148–154.
Archer, G.J., Mundl, A., Walker, R.J., Worsham, E.A., Bermingham, K.R., 2017. High-precision analysis of ^{182}W/^{184}W and ^{183}W/^{184}W by negative thermal ionization mass spectrometry: Per-integration oxide corrections using measured ^{18}O/^{16}O. Int. J. Mass Spectrom. 414, 80–86.
Bermingham, K.R., Worsham, E.A., Walker, R.J., 2018. New insights into Mo and Ru isotope variation in the nebula and terrestrial planet accretionary genetics. Earth Planet. Sci. Lett. 487, 221–229.
Birck, J.L., Barman, M.R., Capmas, F., 1997. Re-Os isotopic measurements at the femtomole level in natural samples. Geostandards Newsletter 21 (1), 19–27.
Brasser, R., Mojzsis, S.J., 2020. The partitioning of the inner and outer Solar System by a structured protoplanetary disk. Nat. Astron 4 (5), 492–499.
Buchwald, V. F. 1975. Handbook of Iron Meteorites. University of California Press, 1418. pp. evols.library.manoa.hawaii.edu/handle/10524/35673.
Budde, G., Burkhardt, C., Brennecka, G.A., Fischer-Gödde, M., Kruijer, T.S., Kleine, T., 2016. Molybdenum isotopic evidence for the origin of chondrules and a distinct genetic heritage of carbonaceous and non-carbonaceous meteorites. Earth Planet. Sci. Lett. 454, 293–303.
Budde, G., Burkhardt, C., Kleine, T., 2019. Molybdenum isotopic evidence for the late accretion of outer Solar System material to Earth. Nat. Astron 3 (8), 736–741.
Burkhardt, C., Kleine, T., Oberli, F., Pack, A., Bourdon, B., Wieler, R., 2011. Molybdenum isotope anomalies in meteorites: constraints on solar nebula evolution and origin of the Earth. Earth Planet. Sci. Lett. 312 (3–4), 390–400.
Chabot, N.L., 2004. Sulfur contents of the parental metallic cores of magmatic iron meteorites. Geochim. Cosmochim. Acta 68 (17), 3607–3618.
Chabot, N.L., Zhang, B., 2022. A revised trapped melt model for iron meteorites applied to the IIIAB group. Meteorit. Planet. Sci. 57 (2), 200–227.
Chabot, N.L., Wollack, E.A., McDonough, W.F., Ash, R.D., Saslow, S.A., 2017. Experimental determination of partitioning in the Fe-Ni system for applications to modeling meteoritic metals. Meteorit. Planet. Sci. 52 (6), 1133–1145.
Cohen, A.S., Waters, F.G., 1996. Separation of osmium from geological materials by solvent extraction for analysis by thermal ionisation mass spectrometry. Anal. Chim. Acta 332 (2–3), 269–275.
Cook, D.L., Walker, R.J., Horan, M.F., Wasson, J.T., Morgan, J.W., 2004. Pt-Re-Os systematics of group IIAB and IIIAB iron meteorites. Geochim. Cosmochim. Acta 68 (6), 1413–1431.
Dauphas, N., Davis, A.M., Marty, B., Reisberg, L., 2004. The cosmic molybdenum–ruthenium isotope correlation. Earth Planet. Sci. Lett. 226 (3–4), 465–475.
Fischer-Gödde, M., Becker, H., Wombacher, F., 2010. Rhodium, gold and other highly siderophile element abundances in chondritic meteorites. Geochim. Cosmochim. Acta 74 (1), 356–379.
Fischer-Gödde, M., Burkhardt, C., Kruijer, T.S., Kleine, T., 2015. Ru isotope heterogeneity in the solar protoplanetary disk. Geochim. Cosmochim. Acta 168, 151–171.
Goldstein, J.I., Yang, J., Scott, E.R., 2014. Determining cooling rates of iron and stony-iron meteorites from measurements of Ni and Co at kamacite–taenite interfaces. Geochim. Cosmochim. Acta 140, 297–320.
Hilton, C.D., Bermingham, K.R., Walker, R.J., McCoy, T.J., 2019. Genetics, crystallization sequence, and age of the South Byron Trio iron meteorites: New insights to carbonaceous chondrite (CC) type parent bodies. Geochim. Cosmochim. Acta 251, 217–228.
Hilton, C.D., Ash, R.D., Walker, R.J., 2022. Chemical characteristics of iron meteorite parent bodies. Geochim. Cosmochim. Acta 318, 112–125.
Hirschmann, M.M., Bergin, E.A., Blake, G.A., Ciesla, F.J., Li, J., 2021. Early volatile depletion on planetesimals inferred from C-S systematics of iron meteorite parent bodies. Proc. Natl. Acad. Sci. 118 (13).
Horan, M.F., Walker, R.J., Morgan, J.W., Grossman, J.N., Rubin, A.E., 2003. Highly siderophile elements in chondrites. Chem. Geol. 196, 5–20.
Hunt, A.C., Ek, M., Schönbächler, M., 2017. Platinum isotopes in iron meteorites: Galactic cosmic ray effects and nucleosynthetic homogeneity in the p-process isotope 190Pt and the other platinum isotopes. Geochim. Cosmochim. Acta 216, 82–95.
Kruijer, T. S., Burkhardt, C., Budde, G., & Kleine, T. 2017. Age of Jupiter inferred from the distinct genetics and formation times of meteorites. In: Proceedings of the National Academy of Sciences, 201704461.
Kruijer, T.S., Fischer-Gödde, M., Kleine, T., Sprung, P., Leya, I., Wieler, R., 2013. Neutron capture on Pt isotopes in iron meteorites and the Hf–W chronology of core formation in planetesimals. Earth Planet. Sci. Lett. 361, 162–172.
Kruijer, T.S., Touboul, M., Fischer-Gödde, M., Bermingham, K.R., Walker, R.J., Kleine, T., 2014a. Protracted core formation and rapid accretion of protoplanets. Science 344 (6188), 1150–1154.
Kruijer, T.S., Kleine, T., Fischer-Gödde, M., Burkhardt, C., Wieler, R., 2014b. Nucleosynthetic W isotope anomalies and the Hf–W chronometry of Ca–Al-rich inclusions. Earth Planet. Sci. Lett. 403, 317–327.
Lichtenberg, T., Drążkowska, J., Schönbächler, M., Golabek, G.J., Hands, T.O., 2021. Bifurcation of planetary building blocks during Solar System formation. Science 371 (6527), 365–370.
Lu, Q., Masuda, A., 1994. The isotopic composition and atomic weight of molybdenum. International Journal of Mass Spectrometry and Ion Processes 130 (1–2), 65–72.
Ludwig, K. R. 2003. Users manual for ISOPLOT/EX, version 3. A geochronological toolkit for Microsoft Excel. Berkeley Geochronology Center Special Publication, (4).
McCoy, T.J., Walker, R.J., Goldstein, J.I., Yang, J., McDonough, W.F., Rumble, D., Chabot, N.L., Ash, R.D., Corrigan, C.M., Michael, J.R., Kotula, P.G., 2011. Group IVA irons: New constraints on the crystallization and cooling history of an asteroidal core with a complex history. Geochimica et Cosmochimica Acta 75 (22), 6821–6843.

Nagai, Y., Yokoyama, T., 2014. Chemical separation of Mo and W from terrestrial and extraterrestrial samples via anion exchange chromatography. Anal. Chem. 86 (10), 4856–4863.
Poole, G.M., Rehkämper, M., Coles, B.J., Goldberg, T., Smith, C.L., 2017. Nucleosynthetic molybdenum isotope anomalies in iron meteorites–new evidence for thermal processing of solar nebula material. Earth Planet. Sci. Lett. 473, 215–226.
Rehkämper, M., Halliday, A.N., 1997. Development and application of new iondashexchange techniques for the separation of the platinum group and other siderophile elements from geological samples. Talanta 44 (4), 663–672.
Rubin, A.E., Zhang, B., Chabot, N.L., 2022. IVA iron meteorites as Late-Stage Crystallization Products Affected by Multiple Collisional Events. Geochim. Cosmochim. Acta 331, 1–17.
Rusk, B., 2009. Laser Ablation ICP-MS in the Earth Sciences: Current Practices and Outstanding Issues. Econ. Geol. 104 (4), 601–602.
Schrader, D.L., Lauretta, D.S., Connolly Jr, H.C., Goreva, Y.S., Hill, D.H., Domanik, K.J., Downs, R.T., 2010. Sulfide-rich metallic impact melts from chondritic parent bodies. Meteorit. Planet. Sci. 45 (5), 743–758.
Scott, E.R., 1977. Composition, mineralogy and origin of group IC iron meteorites. Earth Planet. Sci. Lett. 37 (2), 273–284.
Scott, E.R., 2020. Iron meteorites: Composition, age, and origin. *Oxford Research Encyclopedia of Planetary*. Science 206.
Spitzer, F., Burkhardt, C., Budde, G., Kruijer, T.S., Morbidelli, A., Kleine, T., 2020. Isotopic evolution of the inner solar system inferred from molybdenum isotopes in meteorites. The Astrophysical Journal Letters 898 (1), L2.
Tornabene, H.A., Hilton, C.D., Bermingham, K.R., Ash, R.D., Walker, R.J., 2020. Genetics, age and crystallization history of group IIC iron meteorites. Geochim. Cosmochim. Acta 288, 36–50.
Touboul, M., Walker, R.J., 2012. High precision tungsten isotope measurement by thermal ionization mass spectrometry. Int. J. Mass Spectrom. 309, 109–117.
Trinquier, A., Birck, J.L., Allegre, C.J., 2007. Widespread 54Cr heterogeneity in the inner solar system. Astrophys J 655 (2), 1179.
Vockenhuber, C., Oberli, F., Bichler, M., Ahmad, I., Quitté, G., Meier, M., Halliday, A. N., Lee, D.C., Kutschera, W., Steier, P., Gehrke, R.J., 2004. New Half-Life Measurement of H f 182: Improved Chronometer for the Early Solar System. Phys. Rev. Lett. 93 (17) 172501.
Völkening, J., Köppe, M., Heumann, K.G., 1991. Tungsten isotope ratio determinations by negative thermal ionization mass spectrometry. Int. J. Mass Spectrom. Ion Processes 107 (2), 361–368.
Walker, R.J., 2012. Evidence for homogeneous distribution of osmium in the protosolar nebula. Earth Planet. Sci. Lett. 351, 36–44.
Walker, R.J., McDonough, W.F., Honesto, J., Chabot, N.L., McCoy, T.J., Ash, R.D., Bellucci, J.J., 2008. Modeling fractional crystallization of group IVB iron meteorites. Geochim. Cosmochim. Acta 72 (8), 2198–2216.
Warren, P.H., 2011. Stable-isotopic anomalies and the accretionary assemblage of the Earth and Mars: A subordinate role for carbonaceous chondrites. Earth Planet. Sci. Lett. 311 (1–2), 93–100.
Wasson, J.T., 1999. Trapped melt in IIIAB irons; solid/liquid elemental partitioning during the fractionation of the IIIAB magma. Geochim. Cosmochim. Acta 63 (18), 2875–2889.
Wittig, N., Humayun, M., Brandon, A.D., Huang, S., Leya, I., 2013. Coupled W-Os–Pt isotope systematics in IVB iron meteorites: In situ neutron dosimetry for W isotope chronology. Earth Planet. Sci. Lett. 361, 152–161.
Worsham, E.A., Walker, R.J., Bermingham, K.R., 2016. High-precision molybdenum isotope analysis by negative thermal ionization mass spectrometry. Int. J. Mass Spectrom. 407, 51–61.
Worsham, E.A., Bermingham, K.R., Walker, R.J., 2017. Characterizing cosmochemical materials with genetic affinities to the Earth: genetic and chronological diversity within the IAB iron meteorite complex. Earth Planet. Sci. Lett. 467, 157–166.
Worsham, E.A., Burkhardt, C., Budde, G., Fischer-Gödde, M., Kruijer, T.S., Kleine, T., 2019. Distinct evolution of the carbonaceous and non-carbonaceous reservoirs: Insights from Ru, Mo, and W isotopes. Earth Planet. Sci. Lett. 521, 103–112.
Yokoyama, T., Nagai, Y., Fukai, R., Hirata, T., 2019. Origin and evolution of distinct molybdenum isotopic variabilities within carbonaceous and noncarbonaceous reservoirs. Astrophys J 883 (1), 62.